Article:

Stavrou, AG, Hare, C, Hassanpour, A orcid.org/0000-0002-7756-1506 et al. (1 more author) (2020) Investigation of powder flowability at low stresses by DEM modelling. Chemical Engineering Science, 211. 115307. ISSN 0009-2509

https://doi.org/10.1016/j.ces.2019.115307

Investigation of powder flowability at low stresses by DEM modelling

Alexandros Georgios Stavrou [a], Colin Hare [a,*], Ali Hassanpour [b], Chuan-Yu Wu [a]

[a] Department of Chemical and Process Engineering, Faculty of Engineering and Physical Sciences, University of Surrey, Guildford, GU2 7XH, UK

[b] School of Chemical and Process Engineering, Faculty of Engineering, University of Leeds, Leeds, LS2 9JT, UK

ABSTRACT

Ball indentation is a technique capable of assessing powder flowability down to very low consolidation stresses (≤ 1 kPa). With this method, powder flowability is determined by measuring the hardness of a powder bed, which allows the unconfined yield strength to be inferred via the constraint factor. The latter is well established for continuum materials, whereas for particulate systems its dependency on stress level and powder properties is not well defined. This work investigates these factors by simulating the ball indentation method using DEM. The constraint factor is shown to be independent of pre-consolidation stress. Constraint factor generally increases with interface energy for relatively cohesionless powders, though not for cohesive powders. An increase in plastic yield stress leads to a decrease in the constraint factor. Increasing the coefficient of interparticle static friction reduces the constraint factor, while increasing the coefficient of inter-particle rolling friction significantly increases the constraint factor.

Keywords:

Powder flowability

Low consolidation stresses

Ball indentation

Shear cell

DEM modelling

1 Introduction

The inability of cohesive powders to flow consistently and reliably constitutes one of the major concerns of industries that deal with bulk solids handling, such as pharmaceuticals, food and fast-moving consumer goods, since it can lead to process downtime and reduced manufacturing efficiency. Therefore, the study of powder flowability is vital, albeit complex, since particulate systems' behaviour is multivariable, depending on both intrinsic particle properties such as particle size, size distribution, shape, density, surface roughness, porosity, cohesive and frictional forces between particles and system properties such as the stresses applied during storage and processing, and strain rate, as well as on external factors such as temperature and humidity (Rios, 2006).

Over the years, there have been a diverse array of techniques developed for assessing powder flowability, which mostly focused on silo and hopper design and/or qualitative assessment of bulk solid flow, yet there is still a limited understanding on precisely how particle properties, stressing conditions and environmental factors affect flowability in a way that could lead to a reliable prediction of powder flow behaviour. None of the flow evaluation methods are universally applicable, since they usually measure a certain property of the powder that reflects the state of the powder in this specific experiment, and therefore their usage is meaningful in limited applications. Nevertheless, shear cells are the most widely accepted quantitative technique, with approaches developed for utilising the measurements for silo and hopper design (Jenike, 1961; 1964). Shear cells operate in the quasi-static regime, typically at moderate to high stresses that exist in large storage bins or hoppers, and measure the shear stress required to initiate flow under a given normal stress, and subsequently allowing the unconfined yield strength to be estimated from the measured yield locus. As with most traditional flowability assessment techniques, they typically fail to evaluate the flow behaviour of cohesive powders at low consolidation stresses (≤ 1 kPa). At such stresses shear cells are normally unable to generate steady-state shear, or the reproducibility of the measurement of unconfined yield strength is greatly reduced, or does not correlate with observed process behaviour (Schulze, 2008; Søgaard *et al.*, 2014). The common practice is to assume linearity for yield loci, which are extrapolated towards zero normal stress, leading to an overestimation of unconfined yield strength and cohesion, since yield loci tend to curve downwards in the region of low stresses (Schulze, 2008). There are many processes of great interest during which granular materials are exposed to such low stresses and their flowability needs to be determined, such as flow in small scale hoppers, filling and dosing of powders in capsules, feeding powders for packing and tableting machines, and dispersion in dry powder inhalers (DPI). Under such stresses, small contact areas exist between constituent particles, and very little particle deformation occurs, leading to a low structural strength (Harnby *et al.*, 1987). An aerated powder needs a lot less energy to make it flow than is required when the same powder is consolidated (Freeman, 2005). For all the aforementioned reasons, there is a need for established methods for powder flow measurement at low stresses, so that the results are generalisable to a broad class of powders. One such technique for assessment of powder flow at low stresses is ball indentation, which was introduced by Hassanpour and Ghadiri (2007), with its operational window being thoroughly established experimentally by Zafar *et al.* (2017) and computationally by Pasha *et al.* (2013). The first step of this method is to create a powder bed inside a cylindrical die (made of low friction material) and consolidate it by uniaxial compression to a desired stress. Then the compressed bed is penetrated by a spherical indenter, whilst its penetration depth and the resulting vertical force are measured until a desired depth is reached, and then the indenter is unloaded (Hassanpour and Ghadiri, 2007), as shown in Fig. 1.

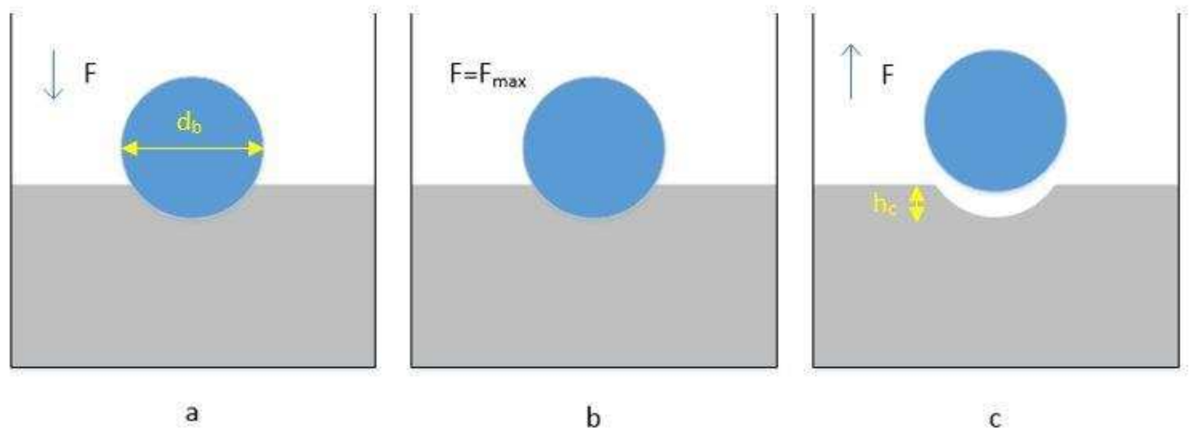

Fig. 1. Indentation step of the procedure.

From the force-displacement response of the powder bed, the hardness of the material is directly measured via Eq. (1), which corresponds to the resistance of the bed to plastic deformation.

$$H = \frac{F_{max}}{A} \quad (1)$$

where F_{max} is the maximum indentation load and *A* is the projected area of the impression of the indenter, calculated from Eq. (2):

$$A = \pi\left(d_b h_c - {h_c}^2\right) \quad (2)$$

where d_b is the indenter diameter and h_c is the indent depth after unloading. If unloading has negligible effect on the material's recovery, the penetration depth at maximum indentation load can be used in place of h_c (Hassanpour and Ghadiri, 2007).

Ball indentation offers the capability of obtaining hardness measurements at any stress level, as long as a flat surface is available for indentation. However, it is commonly of interest to measure the unconfined yield strength, as determined by shear cells. Tabor (1951) demonstrated for continuum materials that for a given material, hardness is directly linked to the yield strength via the constraint factor, *C*, as shown in Eq. (3).

$$H = C\ \sigma_c \quad (3)$$

where σ_c is the unconfined yield strength. The constraint factor represents the phenomenon of plastic constraint seen in penetration tests of continuum solids. The penetration of continuum materials leads to the formation of a local plastic zone around the indenter, where the volume of material under yielding condition is surrounded by an elastically deformed region, which cannot easily flow. This leads to an increase in the local yield strength, represented by the hardness (Kozlov *et al.*, 1995). This phenomenon has been found to be existent in particulate systems as well (Hassanpour and Ghadiri, 2007; Zafar, 2013). In the case of continuum solids, the constraint factor has been stated to have a value of 3 for rigid-perfectly plastic materials (Hill, 1950), while according to Tabor (1951) this value is applicable only for ductile metals. Furthermore, for continuum materials *C* is known to depend on material properties (Tabor, 1996). Johnson (1985) introduced a relationship between indentation hardness and yield strength for elastic-perfectly plastic materials, based on Young's modulus, radius of the impression and the indenter radius. For particle systems the constraint factor doesn't have a fixed value, with different values determined for a variety of powders (Hassanpour and Ghadiri, 2007; Wang *et al.*, 2008; Zafar 2013). Currently the constraint factor of a powder is not known *a priori*, nor is its behaviour throughout a wide stress range, since shear cells cannot be operated at low consolidation stresses. In addition to this, it is unknown which particle properties influence *C*, and to what extent. Shedding light on all of the above is of particular importance, because it will render it possible for Eq. (3) to be utilised to infer unconfined yield strength from ball indentation measurements, which are applicable at low stresses that cannot usually be reached by shear cells (Zafar, 2013).

The Distinct Element Method (DEM) constitutes the most well-established and widely used computational technique capable of describing the mechanical behaviour of particles, since it takes into account the physical and mechanical properties of each individual particle within a system. This can provide fundamental understanding of powder behaviour, with a characteristic example being determination of the internal stresses exerted in a powder bed, which typically cannot be determined experimentally. DEM was first introduced by Cundall (1971) and further developed by Cundall and

Strack (1979). In recent years, the continuous improvement of computer performance and development of rigorous models more accurately representing the true contact mechanics between particles have resulted in a substantial increase in DEM use as a research tool. This has been applied in the field of powder flow, with Hare and Ghadiri (2013), Pasha *et al.* (2013) and Höhner *et al.* (2014) being examples of researchers that have employed DEM simulations on powder flow studies.

In this work, the ball indentation method is simulated using DEM to determine the constraint factor throughout a wide range of low and high pre-consolidation stresses, since the consistency of constraint factor towards low stresses has not been demonstrated elsewhere. Furthermore, the effects of individual particle properties, which cannot be easily modified experimentally, on the constraint factor and the flow resistance are investigated, which until now has not been reported using DEM.

2 DEM simulation setup

EDEM® DEM software provided by DEM Solutions (Edinburgh, UK) is used to simulate the ball indentation system, which is shown in Fig. 2a. The linear elasto-plastic and adhesive contact model of Pasha *et al.* (2014), shown in Fig. 3, is used to represent cohesive powders. This model is a simplified version of the model by Thornton and Ning (1998), which is less computationally expensive. Also, it considers aspects of Tomas (2007), Luding (2008) and Walton and Johnson (2009) models.

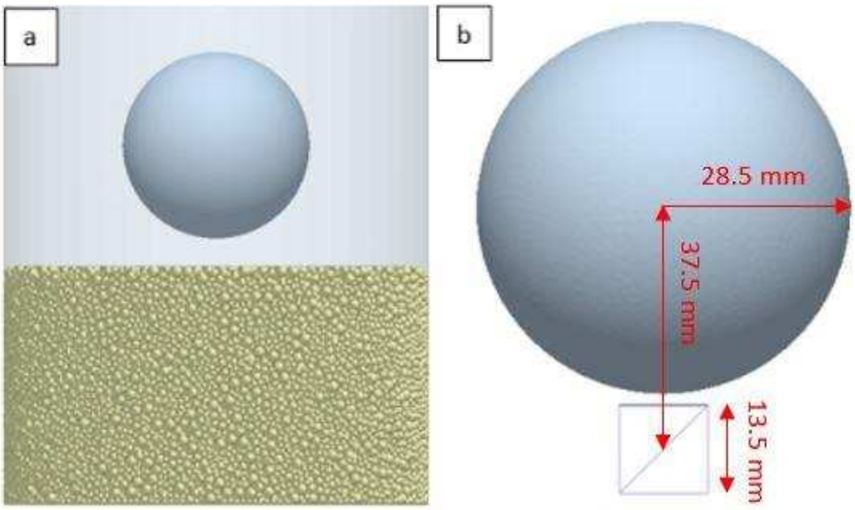

Fig. 2. Ball indentation in EDEM® (a: simulated ball indentation system, b: stress measurement cell).

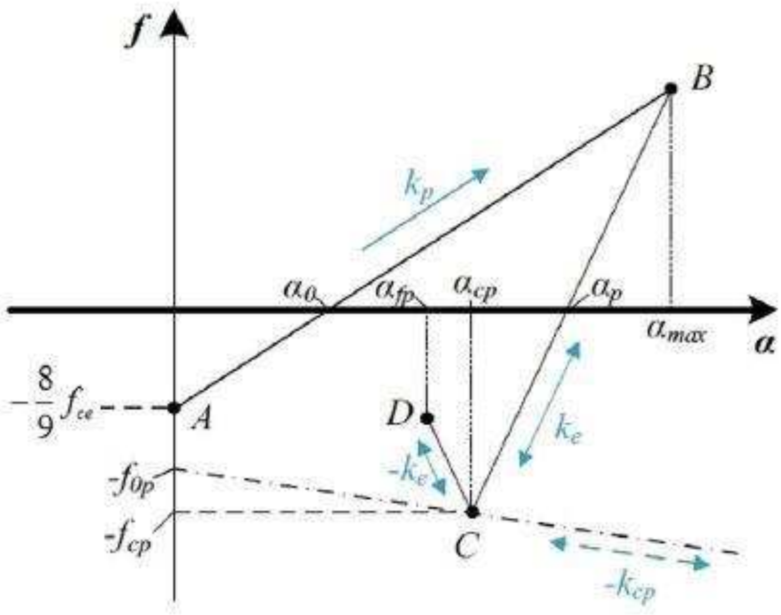

Fig. 3. The Pasha *et al.* (2015) contact model

In this model, once the contact is established at an overlap, *α*, equal to zero (point A), the contact force immediately reduces to a negative force, representing van der Waals forces, with magnitude equal to 8/9 times the JKR elastic pull-off force, f_{ce}, given by Eq. (4) (Johnson *et al.*, 1971):

$$f_{ce} = \frac{3}{2}\pi R^{*}\Gamma \quad (4)$$

where Γ is the interface energy and R^* is the reduced radius computed from Eq. (5):

$$R^* = \left(\frac{1}{R_1} + \frac{1}{R_2}\right)^{-1} \quad (5)$$

where R_1 and R_2 are the radii of the two elements in contact. In case one of the elements in contact is a wall and not a particle, its radius is considered to be infinite (∞).

Initial elastic deformation is ignored and the deformation of the contact is plastic during loading up to the maximum loading force reached at point B, with the contact force, F_n, given by Eq. (6):

$$F_n = k_p a - \frac{8}{9} f_{ce} \quad (6)$$

where k_p is the plastic stiffness.

After a_{max} (point B) is reached, unloading proceeds with elastic stiffness (k_e), reaching first an overlap, a_p, at which point the unloading force becomes zero, with the contact force in this part of the graph given by Eq. (7):

$$F_n = k_e(a - a_p) \quad (7)$$

If reloading occurs, the contact force follows Eq. (7) until point B is reached, beyond which the contact deforms plastically with stiffness k_p. Otherwise, unloading continues until the maximum tensile force, known as the pull-off force, f_{cp}, is reached at an overlap of a_{cp} (point C). Unloading beyond this point is governed by a 'stiffness' equal to -k_e until the contact breaks at an overlap of α_{fp} (point D), with the force being 5/9 times the pull-off force, f_{cp}. On the CD line the contact force is calculated from Eq. (8):

$$F_n = -k_e(a - 2a_{cp} + a_p) \quad (8)$$

The plastic deformation described by this model is reversible. If the two particles come towards each other again after the contact has been broken, the contact is re-established at an overlap slightly larger than α_{cp}, because the particles relax after contact breakage, with the contact force being 8/9 times the pull-off force, f_{cp}. The pull-off force, f_{cp}, and the overlap at contact breakage, α_{fp}, are determined based on the interface energy, Γ, the reduced radius (R^*), the elastic stiffness (k_e) and the maximum contact force, f_{max}, which is achieved at the maximum overlap, a_{max} (point B). As the degree of plastic deformation, α_{cp}, increases, so does the pull-off force. For computational cost-efficiency purposes, the linearised version of the contact model's pull-off force curve is used in this work, where the pull-off force is given by Eq. (9):

$$f_{cp} = -k_{cp}a_{cp} + f_{0p} \quad (9)$$

where k_{cp} is the slope of the linear fit to the pull-off force curve and f_{0p} is the intercept of the fit with the force axis (see Pasha *et al.* (2014) for further detail).

For tangential displacement, the tangential stiffness, F_t, is taken to be linear, and is given by Eq. (10):

$$F_t = k_t a_t \quad (10)$$

where k_t is the tangential stiffness at the contact and a_t is the tangential overlap.

The criteria for sample, die and indenter dimensions established by Pasha (2013) and Zafar (2013) are adhered to in this work. The indenter velocity is set to 0.057 m/s during loading and unloading, which results in a strain rate of 2 s^{-1}, assuming strain rate is equal to indenter velocity divided by indenter radius. This corresponds to a dimensionless strain rate of around 0.03 according to Eq. (11) introduced by Tardos *et al.* (2003), therefore testing in the slow, frictional regime.

$$\gamma^{o*} = \gamma^{o}\sqrt{\frac{d_p}{g}} \quad (11)$$

where $\gamma^{o}*$ is the dimensionless shear strain rate, γ^{o} is the shear strain rate, d_p is the particle diameter and g is the gravitational acceleration.

Around 68 000 spherical particles of 33.3 % w/w 1 mm, 33.3 % w/w 1.43 mm and 33.3 % w/w 1.86 mm radius were generated inside a cylindrical die of 65 mm radius and 500 mm height, with an initial downward velocity of 0.5 m/s, and allowed to settle under gravity, so that a powder bed height of approximately 72 mm is obtained. The particles created were given a size distribution in order to avoid ordered packing. Once the particles had settled, which is indicated by their average velocity having reached a negligible value (≈ 0.001 m/s), a cylindrical piston of 65 mm radius was generated above the powder bed, and driven downwards at a velocity of 0.057 m/s until contact was made, at which point a servo-control mechanism modified the piston velocity until the target vertical stress was achieved. The target stress was maintained for a short period (0.2 - 0.3 s), before unloading the piston at the same velocity until the vertical stress reached zero, and finally removing it from the simulation. Following this consolidation step, a 28.5 mm radius spherical indenter was generated above the consolidated powder bed, and driven downwards at the same velocity as the piston until a penetration depth of approximately 26 mm was obtained.

All the particles simulated were given properties similar to nylon, having a particle density of 1,000 kg/m^3, a Young's modulus of 2 GPa and a Poisson's ratio of 0.25. The properties of both particle-particle and particle-wall interactions that were used for all simulations are shown in Table 1, with the particle-particle and particle-wall values reported referring to the values given for the interactions between two mid-sized particles, and a mid-sized particle and the geometries, respectively.

Table 1. Properties used in DEM simulations (default values indicated in bold).

Symbol	Property	Particle-Particle	Particle-Wall
k_e (kN/m)	Elastic stiffness	165	165

k_p (kN/m)	Plastic stiffness	100	100
k_t (kN/m)	Tangential stiffness	165	165
k_{cp} (kN/m)	Slope of the linear fit to the pull-off force of Pasha *et al.* curve	1.43	0
f_0 (N)	Contact force at zero overlap	-0.117	0
f_{0p} (N)	Intercept of the linear fit to the pull-off force with the force axis	-0.0148	0
e (-)	Coefficient of restitution	0.3	0.3
μ_s (-)	Coefficient of static friction	0.1, **0.3**, 0.5	0.1
μ_r (-)	Coefficient of rolling friction	**0.01**, 0.05, 0.1	0.01
Γ (J/m^2)	Interface energy	1, 2, **5**, 10, 20	0
σ_y (MPa)	Plastic yield stress	11.25, 22.5, **45**	-

The default values for the coefficients of restitution, static friction and rolling friction werechosen to be close to the ones used in the work of Pasha (2013). The rolling friction model used in this work is the standard rolling friction model of EDEM®. The radii, Young's moduli and Poisson's ratios of the two particles in contact, along with the interface energy and the plastic yield stress, are direct inputs for a proprietary MATLAB code provided by Dr. Massih Pasha (The Chemours Company) that was used to compute k_e, k_p, k_t, k_{cp}, f_0 and f_{0p}, which in turn are inputs for the contact model used. Since each simulation contains a range of particle sizes, the different interface energy between particles of different radii needs to be considered. In this regard, the interface energy of particles of different size was scaled following the recommendation of Thakur *et al.* (2016) using Eq. (12).

$$\Gamma_{p2}/\Gamma_{p1} = (R_{p2}/R_{p1})^2 \quad (12)$$

where Γ_{p1}, Γ_{p2} and R_{p1}, R_{p2}, are the values of interface energy and the radii of particle size 1 and particle size 2, respectively. Subsequently, the stiffness values, f_0 and f_{0p} changed with size.

In each simulation the integration time-step, t_{sim}, was computed based on a mass-spring system by Eq. (13) (Pasha, 2013):

$$t_{sim} = 0.2\sqrt{\frac{m_{smallest}}{k_{largest}}} \quad (13)$$

where $m_{smallest}$ is the mass of the smallest particle in the system and $k_{largest}$ is the largest stiffness in the system.

In all simulations carried out throughout this work, hardness was calculated using Eq. (1). For the calculation of the projected area of the impression of the indenter (Eq. (2)), the penetration depth at maximum indentation load was considered, assuming unloading has negligible effect on the simulated material's bed recovery. A 13.5 mm length cubic measurement cell (containing approximately 90 - 590 particles) was created directly beneath and centrally aligned with the indenter, and its position was fixed relative to the indenter (Fig. 2b). The forces acting on every particle whose centre is within the measurement cell were calculated, and the *ij*-component of the stress tensor in the measurement cell, σ_{ij}, was determined following the approach of Bagi (1996) via Eq. (14):

$$\sigma_{ij} = -\frac{1}{V_m}\sum_{N_p}\sum_{N_c}\left|x_i^c - x_i^p\right| n_i F_j \quad (14)$$

where V_m is the volume of the measurement cell, N_p is the number of particles in the measurement cell, N_c is the number of contacts around particle *p*, x_i^c, x_i^p and n_i are the *i*-components of contact location, particle centre location and normal vector directed from a particle centroid to its contact, respectively, and F_j is the *j*-component of the contact force. The term $|x_i^c - \mathrm{xi}^\mathrm{p}|$ is approximately equal to the particle radius, therefore is replaced by particle radius in Eq. (14).

The deviatoric stress, τ_D, corresponding to the shear stress, was calculated using Eq. (15):

$$\tau_D = \sqrt{\frac{(\sigma_1 - \sigma_3)^2 + (\sigma_1 - \sigma_2)^2 + (\sigma_3 - \sigma_2)^2}{6}} \quad (15)$$

where σ_1, σ_2 and σ_3, are the major, intermediate and minor principal stresses, respectively, which were determined from the nine components of the stress tensor.

In order to determine the constraint factor, it is necessary to know the hardness and the unconfined yield strength. The hardness can be determined in the DEM simulations using Eq. (1), however the unconfined yield strength cannot be determined in the ball indentation simulations. As such, an alternative method is needed. Stavrou (2019) experimentally assessed the flowability of a wide range of powders in the FT4 shear cell. Fig. 4 shows the shear stresses and unconfined yield strengths of measurements using a pre-shear stress of 6 kPa and applied stresses of 1, 2, 3, 4 and 5 kPa, for 63 - 75 µm silanised glass beads (S), alumina CT800SG (A), limestone (L) and maize starch (M). There is a strong, approximately linear, relationship between the shear stress and the unconfined yield strength, particularly at the lower applied stress of 1 kPa, which is closer to the failure Mohr circle. Therefore, the term *C′* is used instead of the constraint factor, by using the deviatoric (shear) stress in place of the unconfined yield strength, as shown in Eq. (16):

$$C' = \frac{H}{\tau_D} \quad (16)$$

It is noted that *C′* will be larger than *C*, since deviatoric stress close to the failure Mohr circle (1 kPa in Fig. 4) is smaller than unconfined yield strength, however it is proportional to *C*. Therefore, any trends observed for *C′* also apply to *C*.

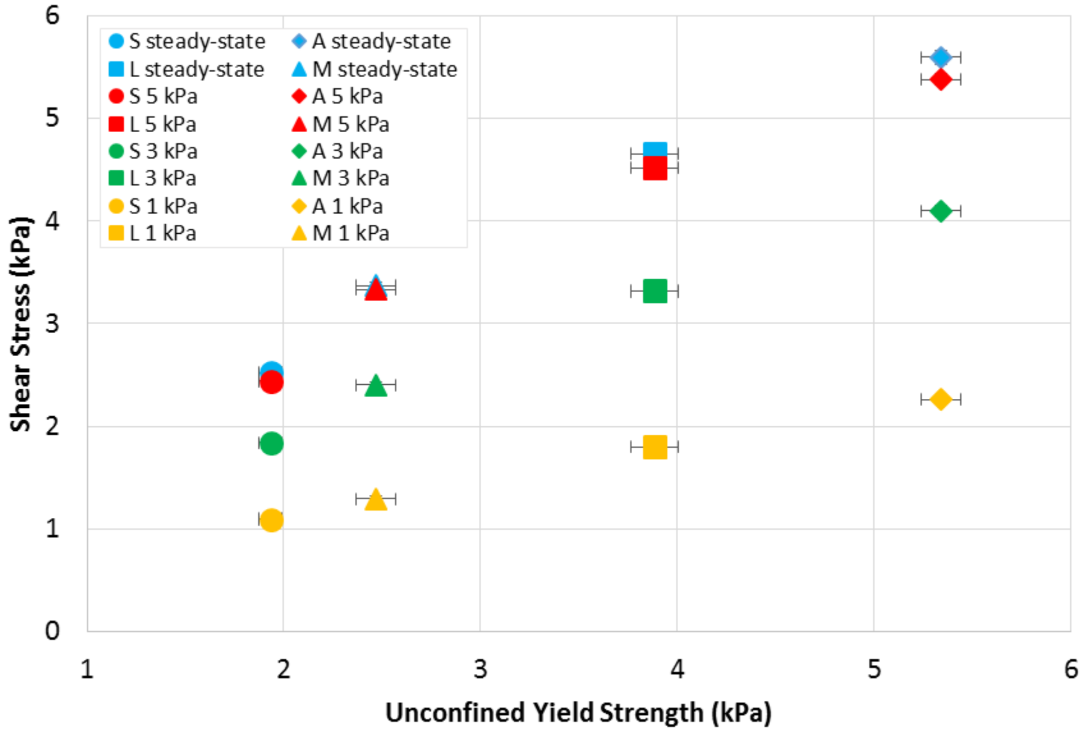

Fig. 4. Shear stress vs unconfined yield strength at a pre-shear normal stress of 6 kPa, showing steady-state and three points of incipient failure (first, third and fifth point). For 63 - 75 µm silanised glass beads, alumina CT800SG, limestone and maize starch, the abbreviations S, A, L and M are used respectively in the legend of this Figure.

3 Results and discussion

3.1 Effect of consolidation stress

In order to assess the behaviour of the constraint factor as a function of the applied stress, five different stresses, namely 0.1, 0.5, 1, 5 and 10 kPa, were applied to consolidate the powder bed prior to indentation. The default values of particle-particle and particle-wall interactions, highlighted in bold in Table 1, were used for all five simulations. Fig. 5 shows hardness against penetration depth based on the penetration depth at maximum indentation load, h_m, which is non-dimensionalised via Eq. (17) and presented as dimensionless penetration depth, h_d, in the range of 0.2 - 0.9, at all five pre-consolidation stresses.

$$h_d = \frac{2h_m}{d_b} \quad (17)$$

Hardness is overestimated at very shallow depths due to the limited number of contacts and therefore inaccuracy in estimating the projected area of the impression, hence the dimensionless penetration depth of 0.2 was considered as the minimum depth for data analysis. Hardness is found to increase with applied stress, and is virtually independent of penetration depth beyond a dimensionless penetration depth of 0.4, though some fluctuations are present. Greater pre-consolidation stresses lead to more tightly packed powder beds, hence hardness increases due to an increased packing fraction, as shown in Fig. 6, where the packing fraction at maximum compression is plotted against pre-consolidation stress. Also, it can be seen that as the pre-consolidation stress is increased, the minimum depth required to reach the stable hardness region increases, with the threshold being a dimensionless penetration depth of about 0.2 and 0.4 in the cases of beds compressed at 0.1 and 10 kPa, respectively.

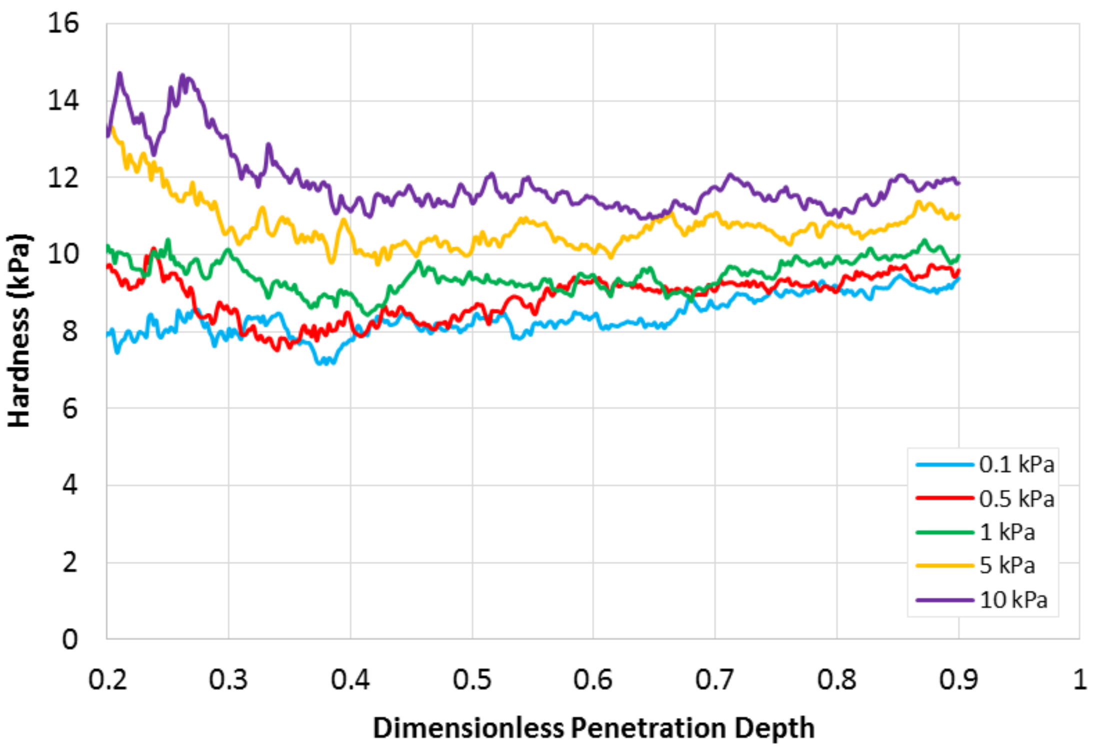

Fig. 5. Hardness against dimensionless penetration depth at five pre-consolidation stresses.

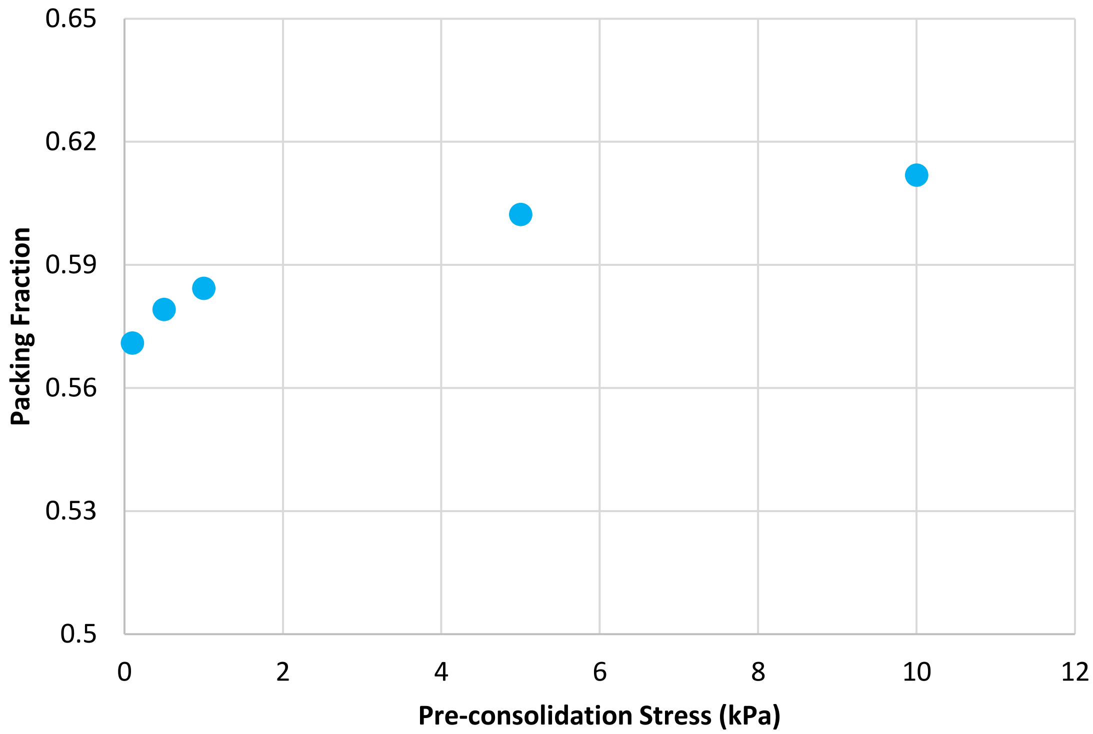

Fig. 6. Packing fraction against pre-consolidation stress.

Fig. 7 shows the deviatoric stress against dimensionless penetration depth for the five pre-consolidation stresses. There is a general increase in deviatoric stress with pre-consolidation stress, while it does not exhibit any general increases or decreases with penetration depth. It is noteworthy that significant fluctuations occur, which are more significant than the fluctuations of hardness. Such fluctuations are common in DEM simulations, due to the sudden changes in force at individual contacts and the high sampling frequency. Simulations could be repeated using different initial particle positions in order to determine average values against depth, and therefore reduce the inherent fluctuations, however the data presented in this work is taken from individual simulations of each condition.

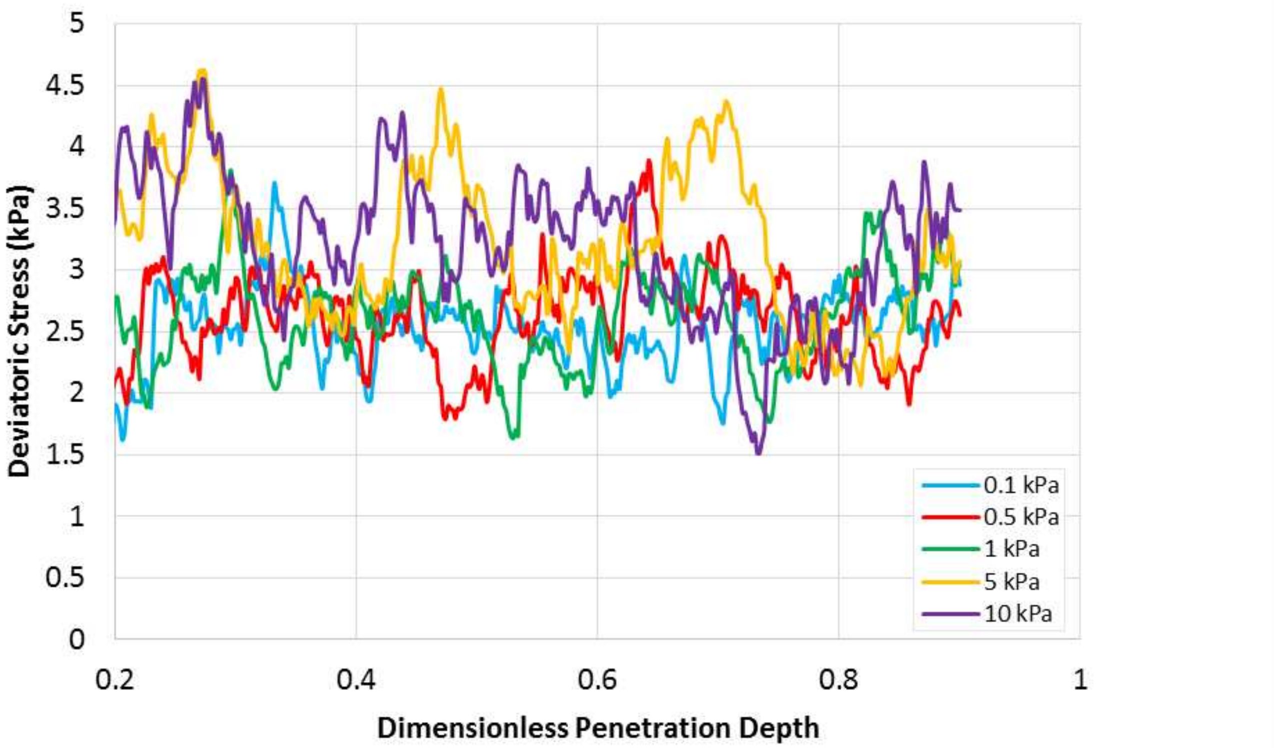

Fig. 7. Deviatoric stress against dimensionless penetration depth at five pre-consolidation stresses.

Using Eq. (16), *C′* was quantified, and is plotted as a function of dimensionless penetration depth at all five pre-consolidation stresses in Fig. 8. *C′* is found to fluctuate around a fixed value for a given pre-consolidation stress, being virtually constant and independent of the pre-consolidation stress applied. In addition to this, the average C′ was calculated through the dimensionless penetration depth range of 0.4 - 0.8, and is presented against pre-consolidation stress in Fig. 9, with error bars showing the standard deviation throughout this penetration depth range. Fig. 9 confirms that the average *C′* remains relatively constant throughout the range of pre-consolidation stresses. Experimentally it isn't possible to compute *C* at such low stresses (≤ 1 kPa), due to the inability of shear cells to give reliable and repeatable results in this stress range, however constraint factor has been shown experimentally to be independent of stress above this low stress range (Wang *et. al*, 2008; Zafar, 2013). The fact that constraint factor remains constant at low stresses means that it is possible to determine constraint factor from hardness and unconfined yield strength measurements at moderate to high stresses by performing ball indentation and shear cell experiments, respectively, and use the same value of constraint factor in order to infer the unconfined yield strength of powders from ball indentation measurements at low stresses.

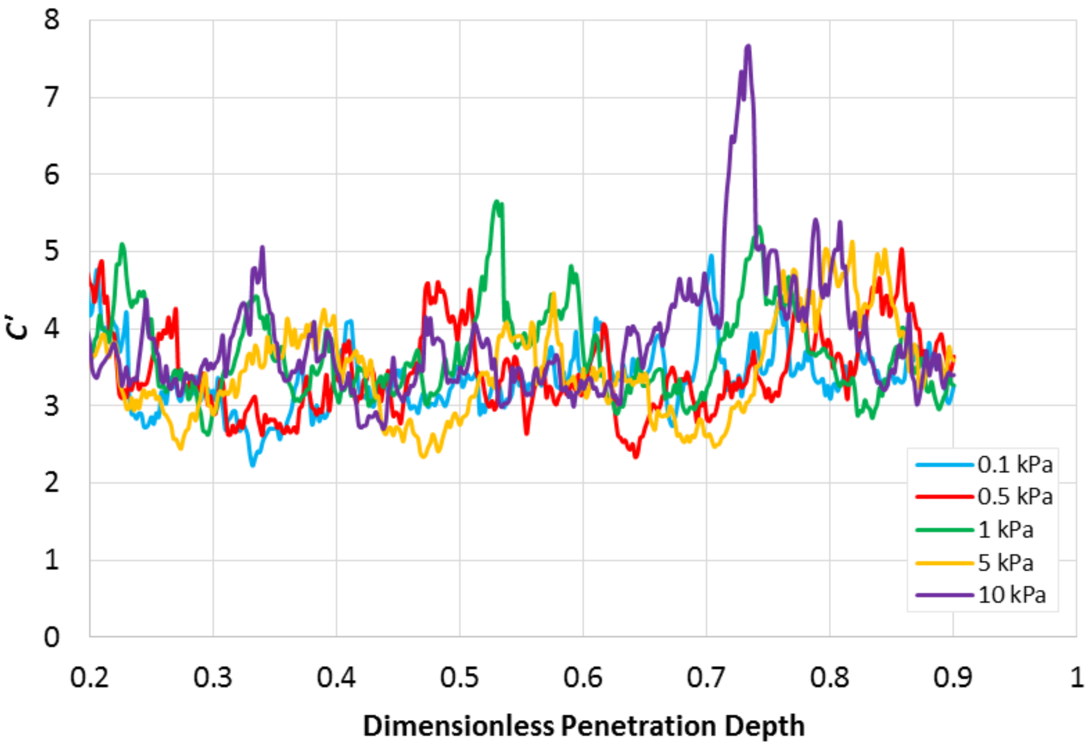

Fig. 8. *C′* against dimensionless penetration depth at five pre-consolidation stresses.

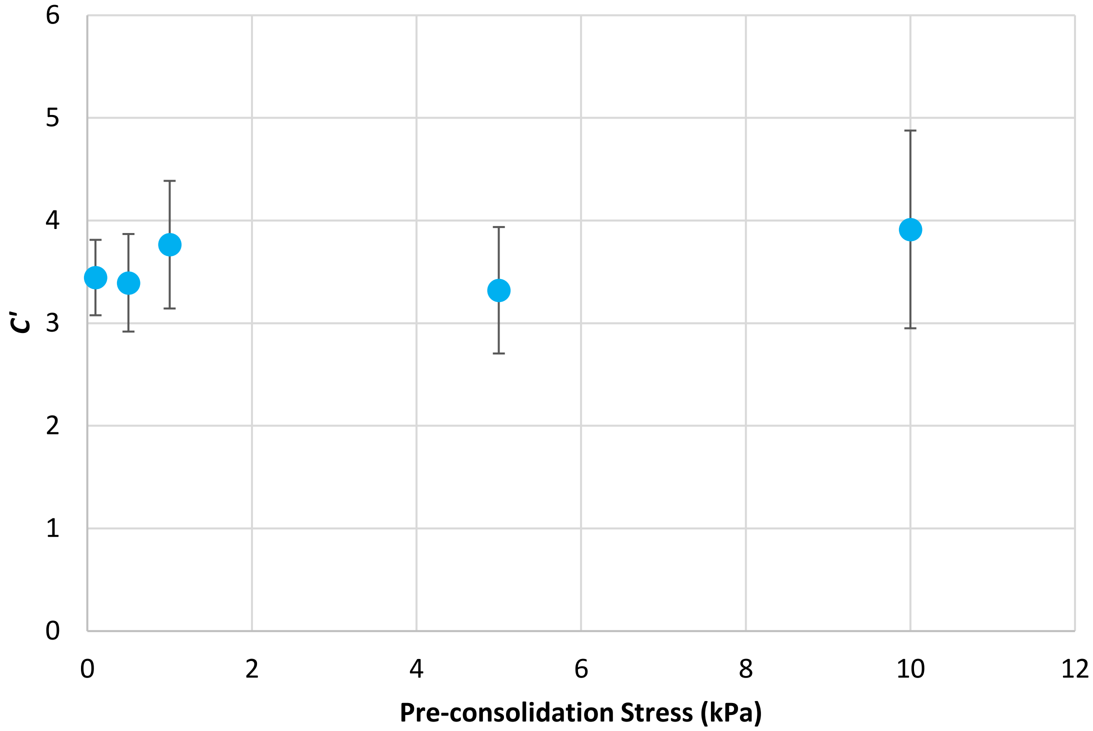

Fig. 9. Average *C′* in the depth range of 0.4 - 0.8 against pre-consolidation stress.

3.2 Effect of interface energy

In this series of simulations, powder beds of five different values of interparticle interface energy, namely 1, 2, 5, 10 and 20 J/m^2, were consolidated at 1 kPa and penetrated by the indenter. These high values of interface energy were chosen due to the large particle size, and correspond to Cohesion numbers, *Coh*, of 0.023 - 3.45 computed from Eq. (18) (Alizadeh *et al.*, 2018), which are equivalent to interface energies of 9 × 10^{-3} to 0.18 mJ/m^2 for 100 µm particles.

$$Coh = \frac{1}{\rho g}\left(\frac{\Gamma^5}{{E^*}^2 {R^*}^8}\right)^{1/3} \quad (18)$$

where ρ is the envelope density of the particles and E^* is the reduced Young's modulus given by Eq. (19):

$$E^* = \left(\frac{1-\nu_1^2}{E_1} + \frac{1-\nu_2^2}{E_2}\right)^{-1} \quad (19)$$

where E_1 and E_2, and v_1 and v_2 are the Young's moduli and Poisson's ratios of the two elements in contact, respectively.

All five simulations were carried out with the default values given in Table 1 (indicated in bold), except for the interparticle interface energy. In Fig. 10 hardness is shown against dimensionless penetration depth for all five values of interface energy. In the case of the two powder beds with the lowest values of interface energy, hardness increases continually with depth. This may indicate that for these relatively cohesionless powders the bed is consolidated during the indentation test, though it is not clear why this is the case. The fact that no stable hardness region is found for these cohesionless powders renders the measurement unreliable. For the middle value of interparticle interface energy, hardness is constant across the whole range of penetration depths, while for the two higher values of interface energy it exhibits the same behaviour beyond a dimensionless penetration depth of around 0.25. An increased interface energy results in greater cohesion, and therefore greater resistance to plastic deformation. The deviatoric stress variation with depth is shown for each interface energy value in Fig. 11. Although notable fluctuations exist, there is an increase of deviatoric stress with increasing interface energy. Qualitatively similar findings have been reported in the work of Pasha (2013).

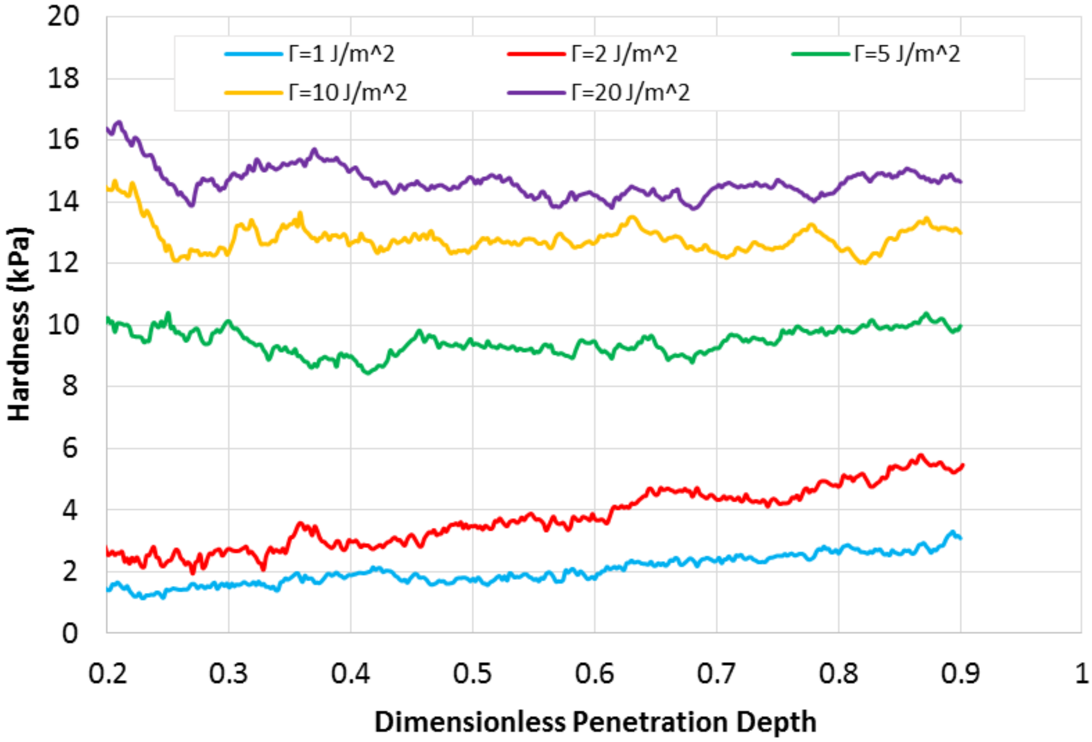

Fig. 10. Hardness against dimensionless penetration depth for five different values of interface energy.

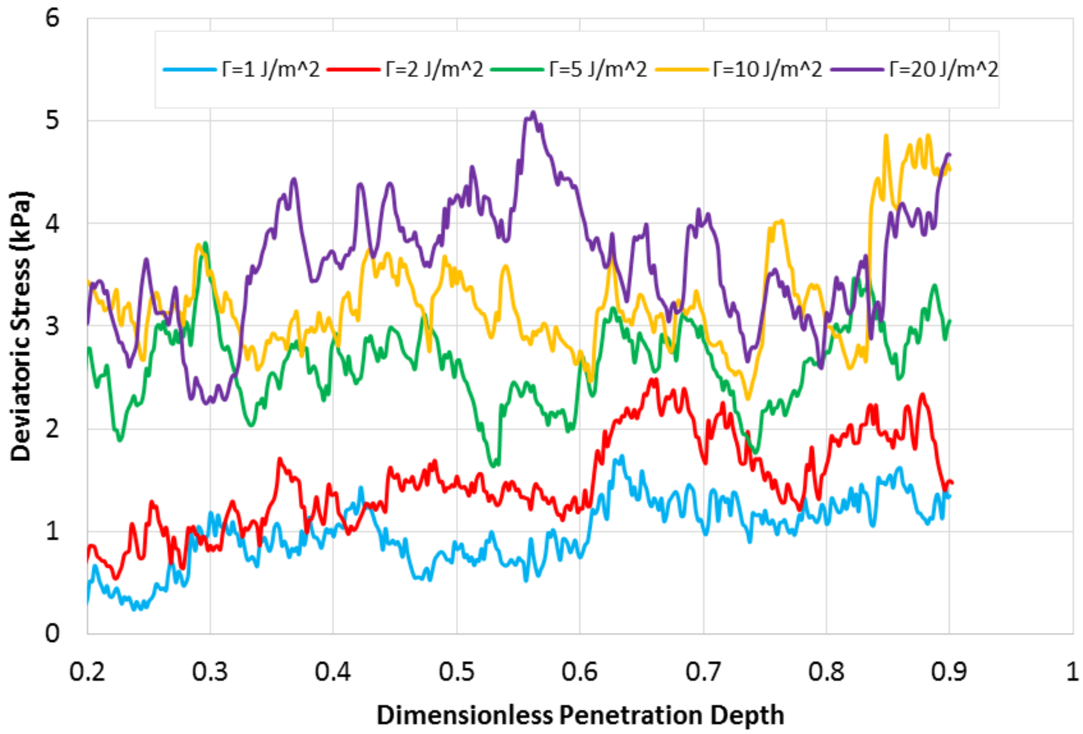

Fig. 11. Deviatoric stress against dimensionless penetration depth for five different values of interface energy.

Fig. 12 shows C' against dimensionless penetration depth, where for a given value of interface energy C' fluctuates around a fixed value beyond a dimensionless penetration depth of 0.4. There is a general increase of C' with interface energy, as the interface energy is increased from 2 to 5 J/m^2. This behaviour is seen more clearly in Fig. 13, where the average value of C' in the dimensionless penetration depth range of 0.4 - 0.8 is presented against interface energy. An increase in interface energy from 1 to 2 J/m^2 leads to a slight increase of C', while a further increase to 5 J/m^2 results in a substantial increase in C', from around 2.5 to around 3.8. It should be noted that 5 J/m^2 is the lowest value of interface energy applied for which the powder bed does not appear to be consolidated during indentation. A further increase of interface energy from 5 to 20 J/m^2 leads to no significant change in the value of C'. This suggests that for powder beds that are sufficiently cohesive to be tested by ball indentation, interface energy does not influence the constraint factor.

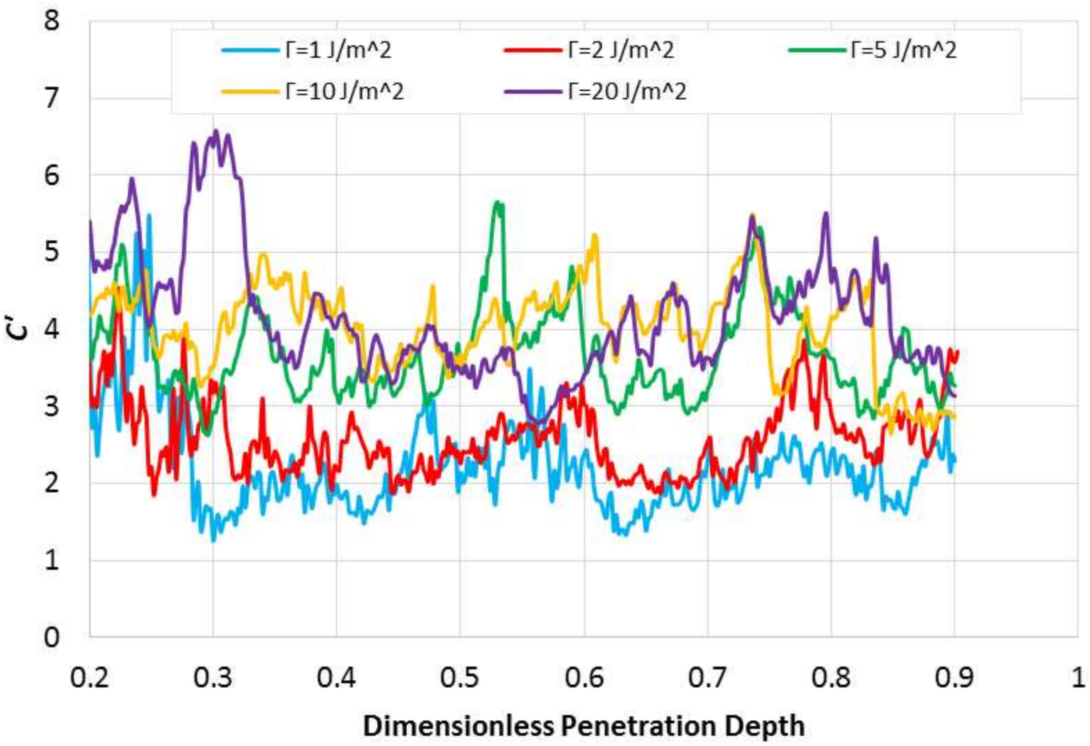

Fig. 12. C' against dimensionless penetration depth for five different values of interface energy.

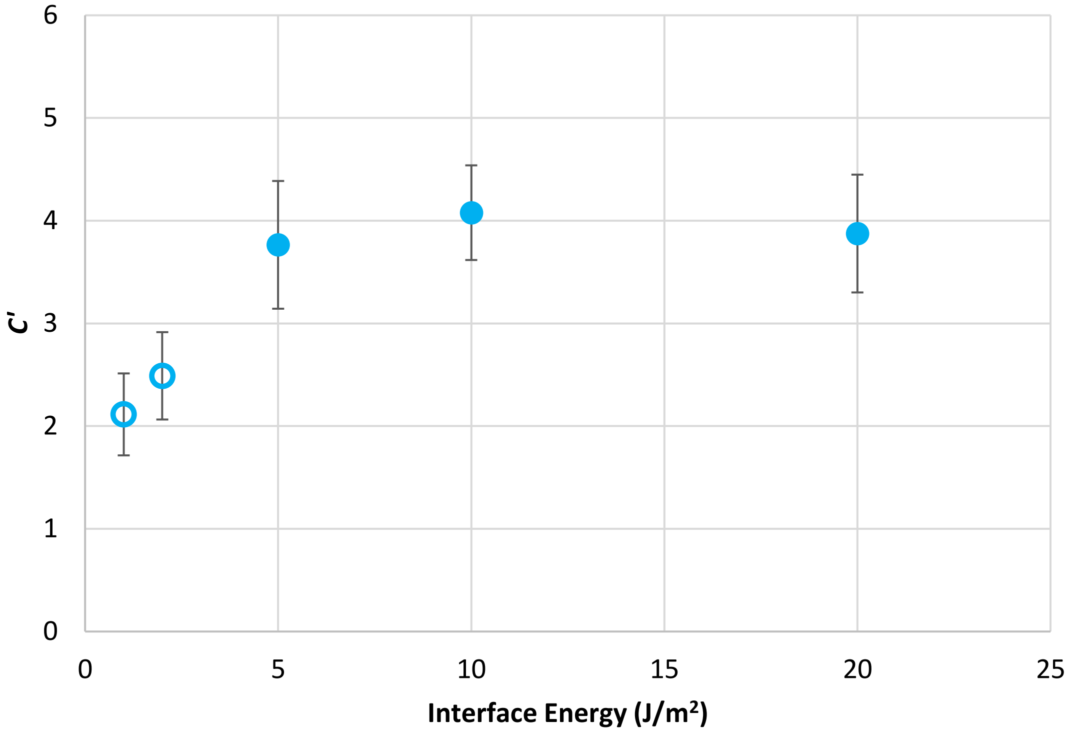

Fig. 13. Average *C′* in the depth range of 0.4 - 0.8 against interface energy.

3.3 Effect of static friction

Three simulations of ball indentation at 1 kPa pre-consolidation stress were run using different values of the coefficient of static friction for interparticle interactions. All the other simulation parameters were given the default values from Table 1. Fig. 14 shows the hardness variation with penetration depth for the different values of static friction coefficient. It can be seen that μ_s values of 0.1 and 0.3 lead to a constant hardness throughout the range of dimensionless penetration depths presented, whereas when the interparticle friction is further increased to 0.5 the hardness is relatively constant in the depth range of 0.3 - 0.5, but then increases notably at a depth of around 0.5, from which point onwards it remains relatively constant. In contrast to this, it can be seen in Fig. 15 that the deviatoric stress fluctuates around a relatively constant value until a dimensionless penetration depth of 0.8, beyond which it increases for all coefficient of static friction values. Also, increasing the static friction coefficient from 0.1 to 0.3 leads to an increase of deviatoric stress, whilst increasing μ_s to 0.5 leads to no further increase. It is expected that increased friction will result in a greater internal resistance to shear deformation, but after a certain level of static friction (μ_s = 0.3 in this case), Coulomb's sliding criterion is not met by the particle's tangential force in certain contacts, and as such contact sliding does not take place. For these non-sliding contacts, a further increase in coefficient of static friction does not lead to any increase in the shear stress, since these contacts remain in a non-sliding condition. This finding agrees with the work of Gröger and Katterfeld (2006) and Pasha (2013), who also showed a limiting μ_s beyond which the shear stress does not increase.

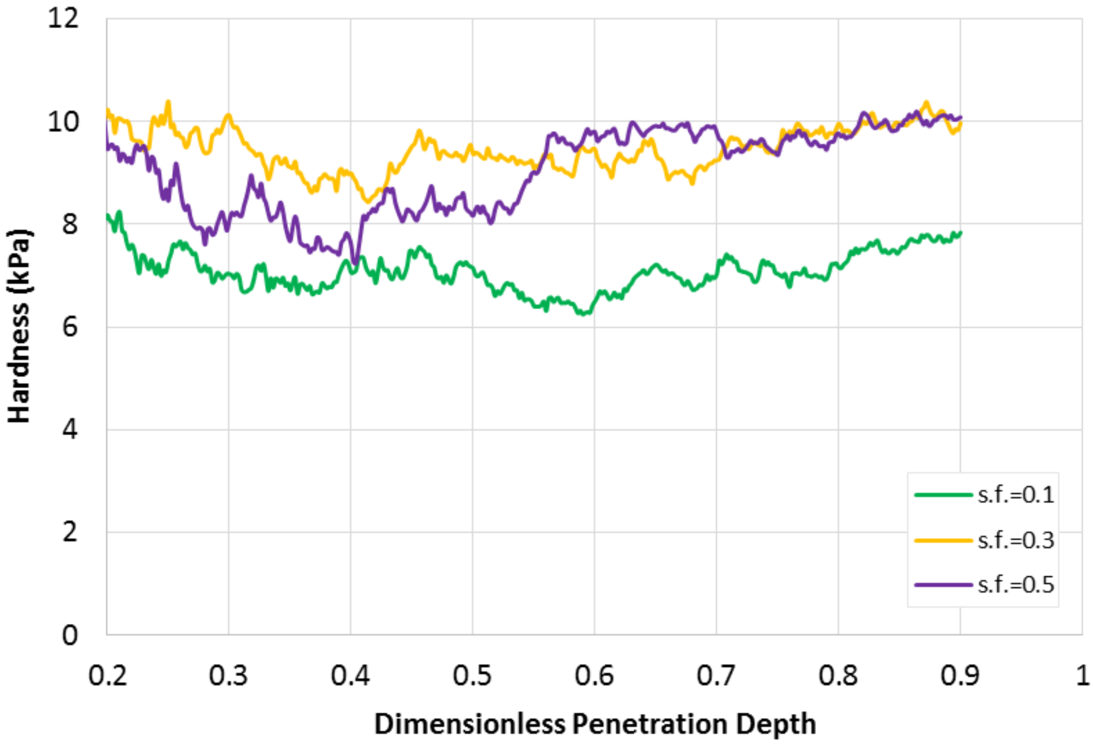

Fig. 14. Hardness against dimensionless penetration depth for three different values of coefficient of static friction.

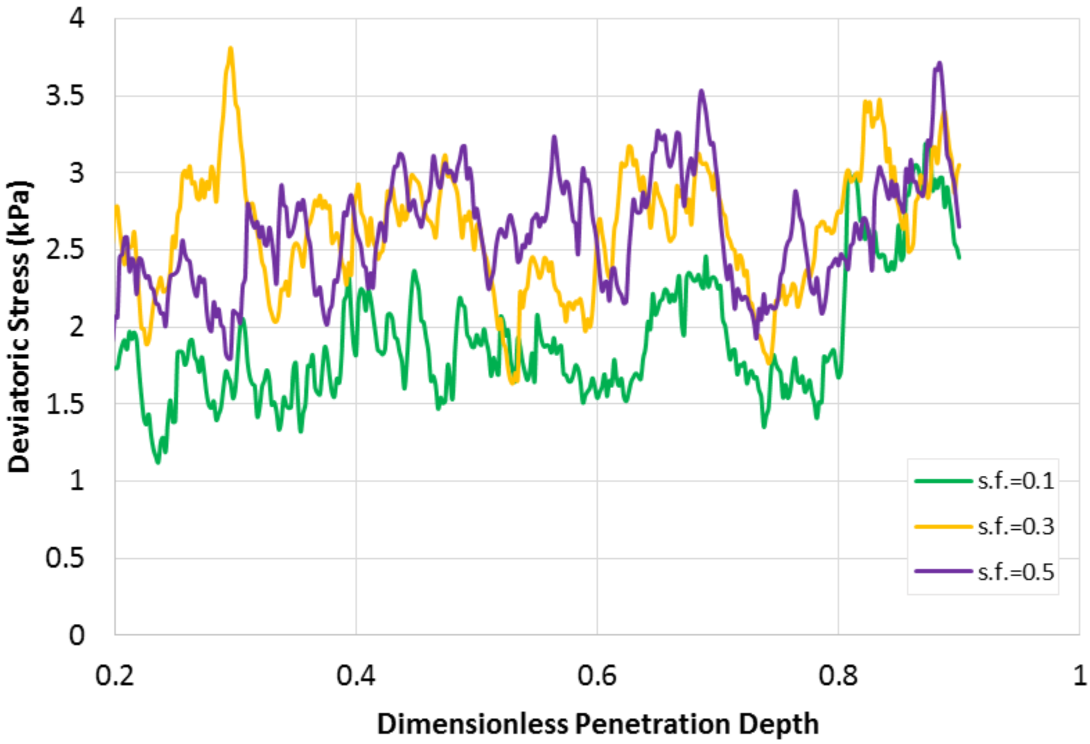

Fig. 15. Deviatoric stress against dimensionless penetration depth for three different values of coefficient of static friction.

Fig. 16 shows *C′* against dimensionless penetration depth for all three values of μ_s. As can be seen, *C′* is relatively constant regardless of the applied penetration depth, but it is not clear whether static friction has any influence on *C′*, since it fluctuates around a similar value for all values of the coefficient of static friction. Fig. 17 shows the average *C′* in the dimensionless penetration depth range of 0.2 - 0.8, which displays a slight reduction with an increase of the coefficient of static friction. However, since the error bars are large, this result is considered to be statistically insignificant.

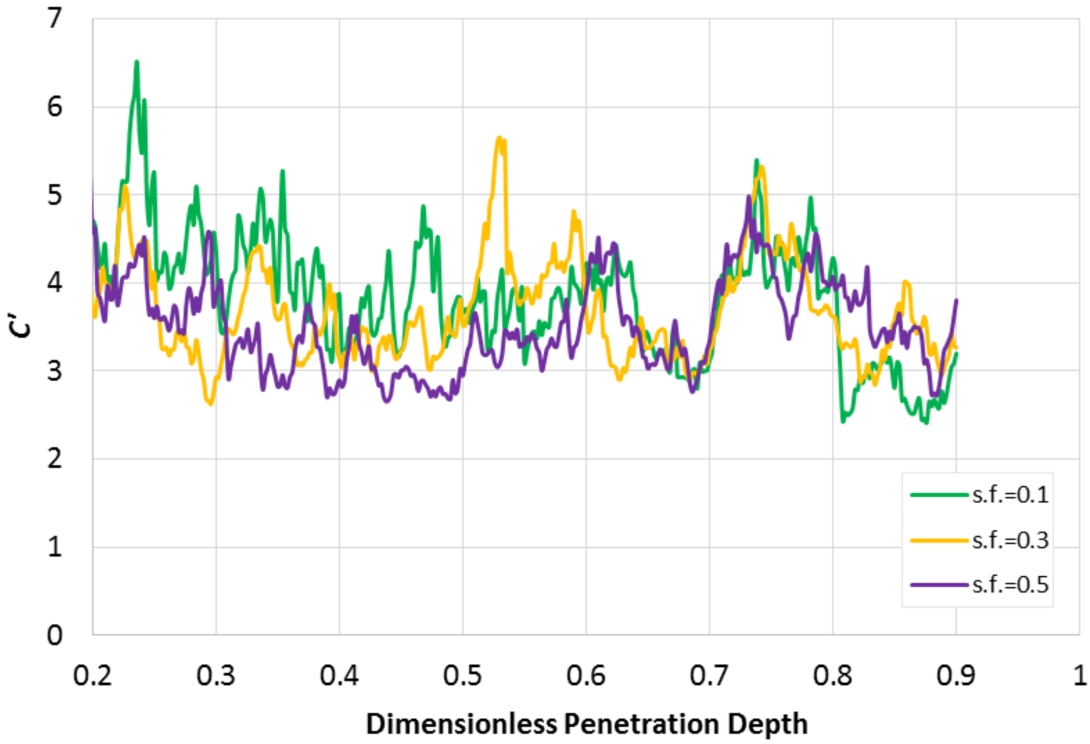

Fig. 16. *C′* against dimensionless penetration depth for three different values of coefficient of static friction.

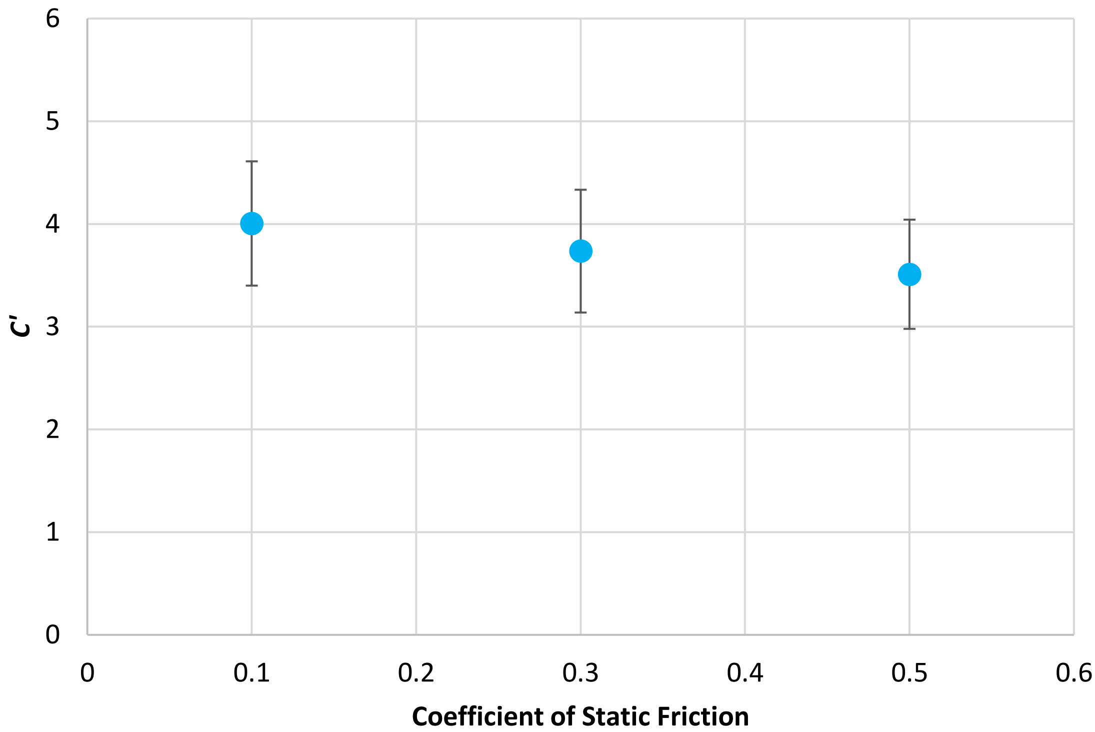

Fig. 17. Average *C′* in the depth range of 0.2 - 0.8 against coefficient of static friction.

3.4 Effect of rolling friction

Ball indentation simulations at 1 kPa pre-consolidation stress were carried out for three different values of coefficient of interparticle rolling friction, whilst the default values from Table 1 were used for the other simulation parameters. Fig. 18 shows that an increase in μ_r from 0.01 to 0.05 leads to an increased hardness, whilst further increase to a value of 0.1 leads to an almost negligible reduction of hardness. In all cases, hardness remains constant beyond a dimensionless penetration depth of 0.4. Fig. 19 shows that the deviatoric stress exhibits the same behaviour against penetration depth as hardness, whilst it shows that increasing the rolling friction coefficient from 0.01 to 0.05 results in a slight increase of the shear stress, but further increasing it to 0.1 results in a clear reduction of shear stress. This reduction in shear stress could be due to a decrease in packing fraction, which translates to a smaller force required for shearing.

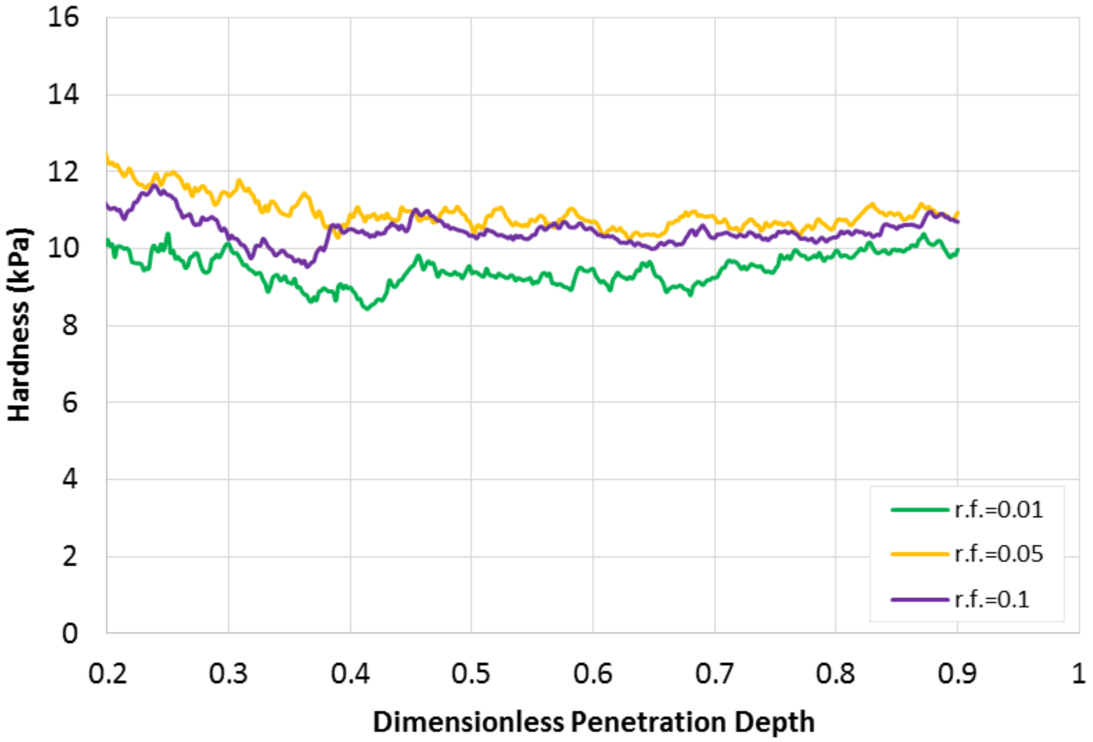

Fig. 18. Hardness against dimensionless penetration depth for three different values of coefficient of rolling friction.

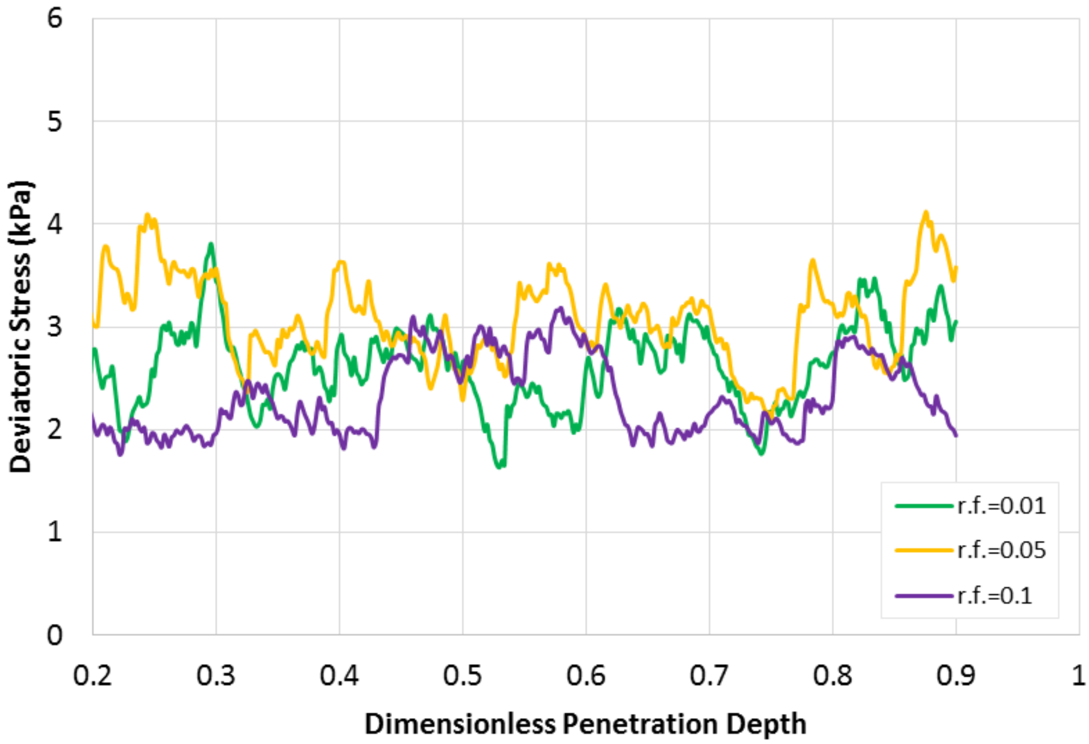

Fig. 19. Deviatoric stress against dimensionless penetration depth for three different values of coefficient of rolling friction.

For all values of coefficient of rolling friction, *C′* is observed to fluctuate around a fixed value throughout the range of applied penetration depths, with the fluctuations being larger for $\mu_r = 0.1$ (Fig. 20). The average *C′* value in the range of 0.4 - 0.8 dimensionless penetration depth is found to be independent of the coefficient of rolling friction as it is increased from 0.01 to 0.05, and then to substantially increase from around 3.5 to around 4.5 with a further increase of μ_r to a value of 0.1 (Fig. 21).

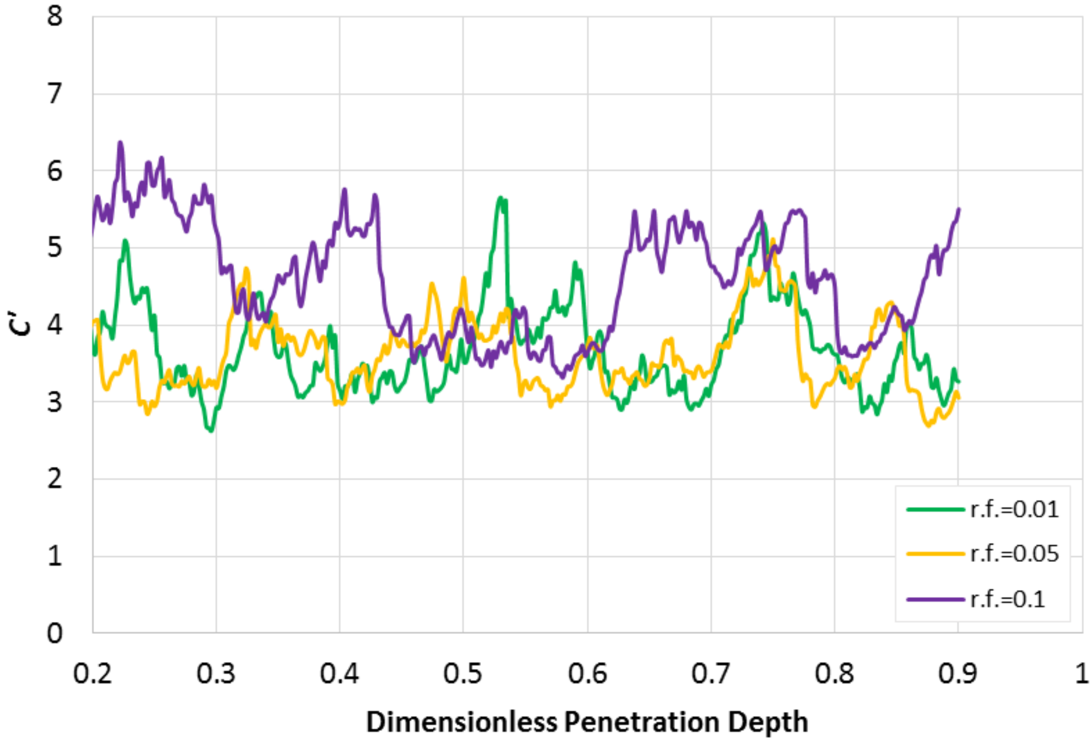

Fig. 20. *C′* against dimensionless penetration depth for three different values of coefficient of rolling friction.

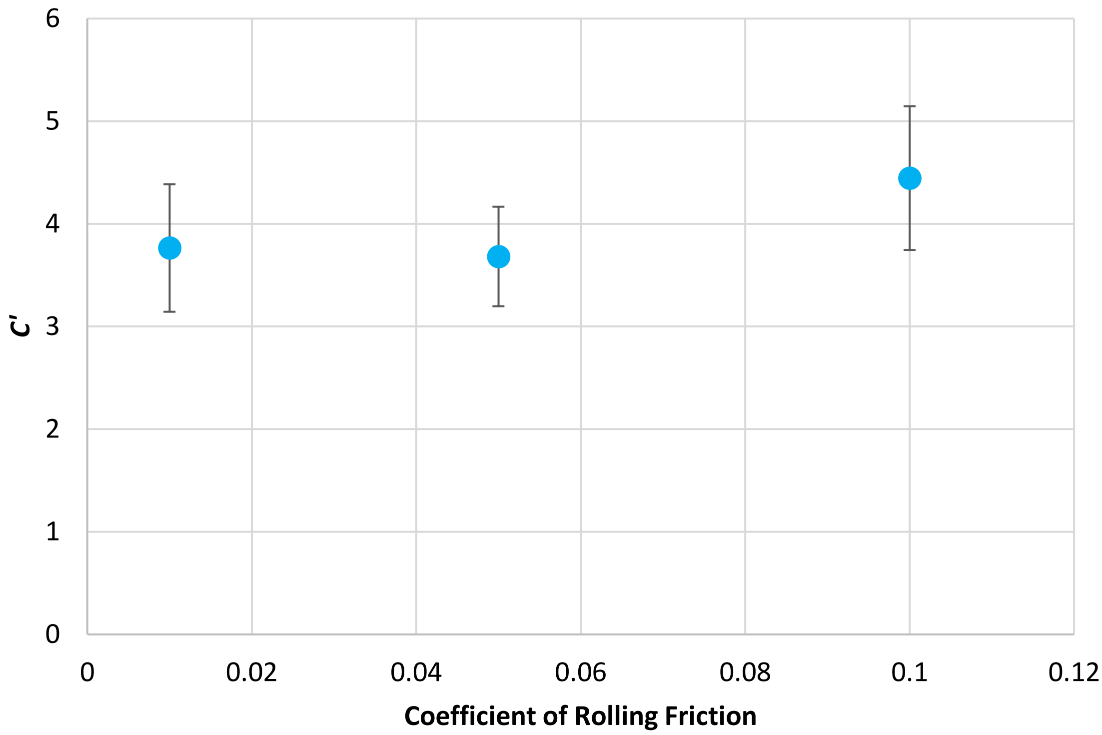

Fig. 21. Average *C′* in the depth range of 0.4 - 0.8 against coefficient of rolling friction.

3.5 Effect of plastic yield stress

Ball indentation simulations at 1 kPa pre-consolidation stress were carried out for three different values of plastic yield stress (σ_y), while all other parameters were given the default values from Table 1. The hardness variation with penetration depth is shown for the different values of σ_y in Fig. 22. Fig. 22 shows that as the plastic yield stress is increased the hardness decreases, which can be explained as follows. Since a higher plastic yield stress means that a greater stress needs to be overcome in order for plastic deformation to initiate, then the number of particles which plastically deform, and therefore create cohesive contacts, decreases. Therefore, since fewer cohesive contacts exist for higher plastic yield stress, then the hardness of the bed is lower. In addition to this, hardness is seen to remain relatively constant with depth for all values of σ_y. In contrast to hardness, the exerted shear stresses do not seem to be influenced by the plastic yield stress, as indicated in Fig. 23.

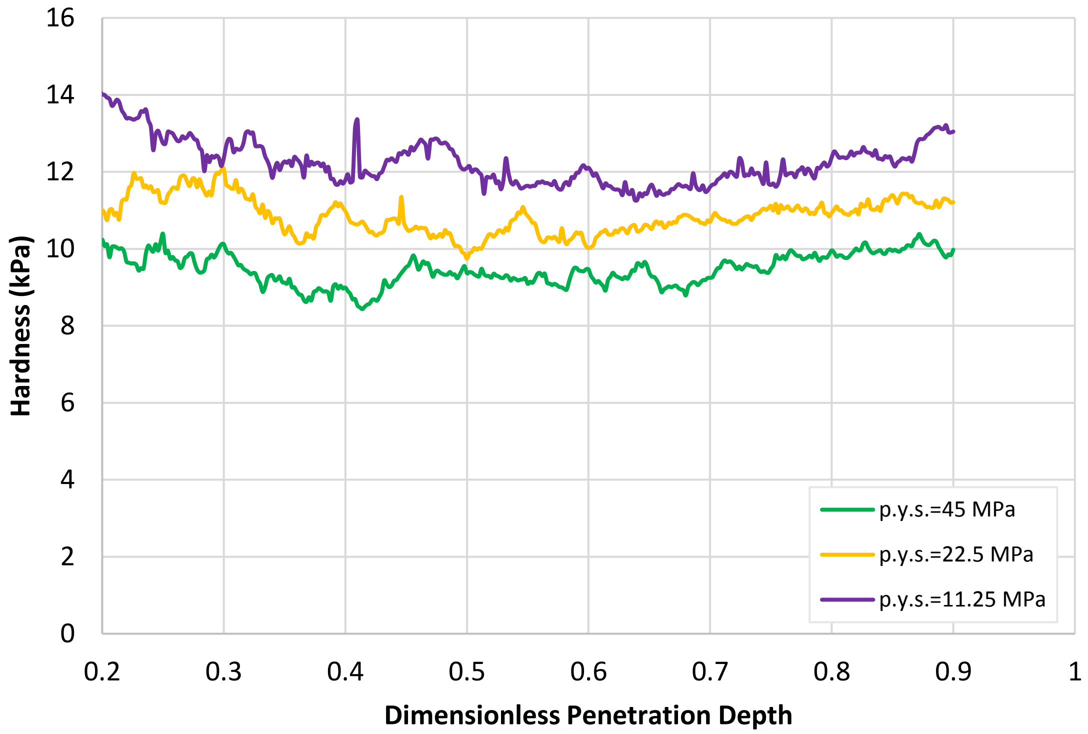

Fig. 22. Hardness against dimensionless penetration depth for three different values of plastic yield stress.

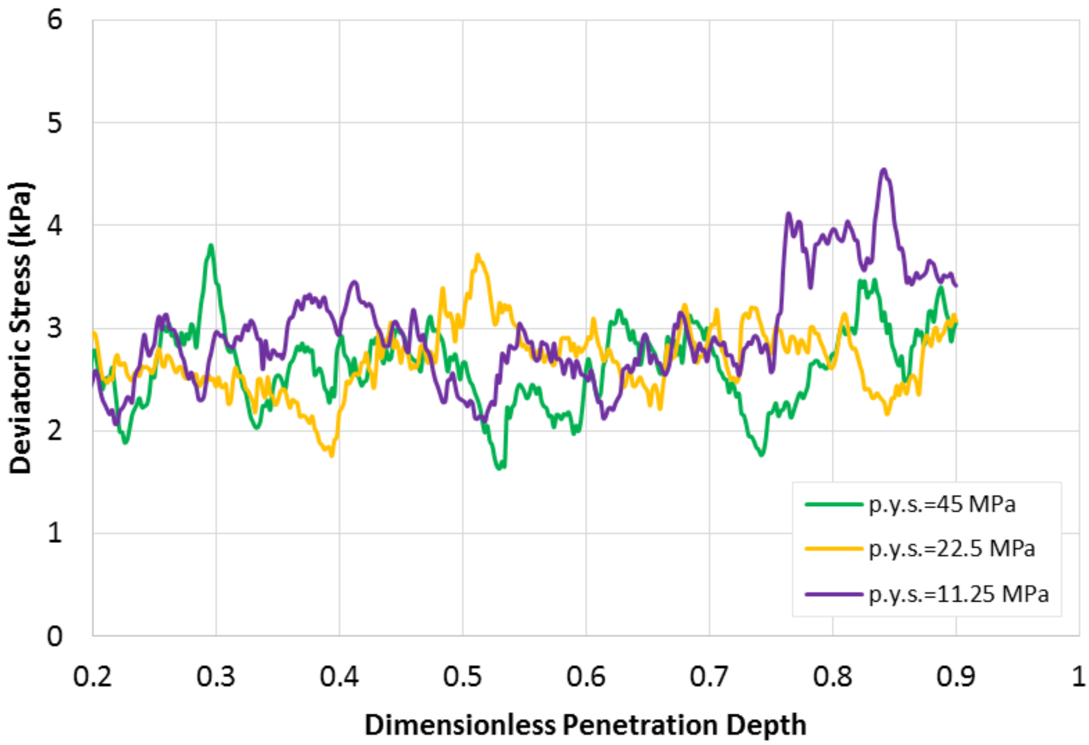

Fig. 23. Deviatoric stress against dimensionless penetration depth for three different values of plastic yield stress.

C′ is plotted against dimensionless penetration depth in Fig. 24, and is shown to be relatively constant across the whole range of penetration depths, regardless of the plastic yield stress. Furthermore, in Fig. 25 the average *C′* in the range of 0.2 - 0.8 dimensionless penetration depth is depicted against plastic yield stress, and is found to decrease with the increase of plastic yield stress, though noticeable error is present.

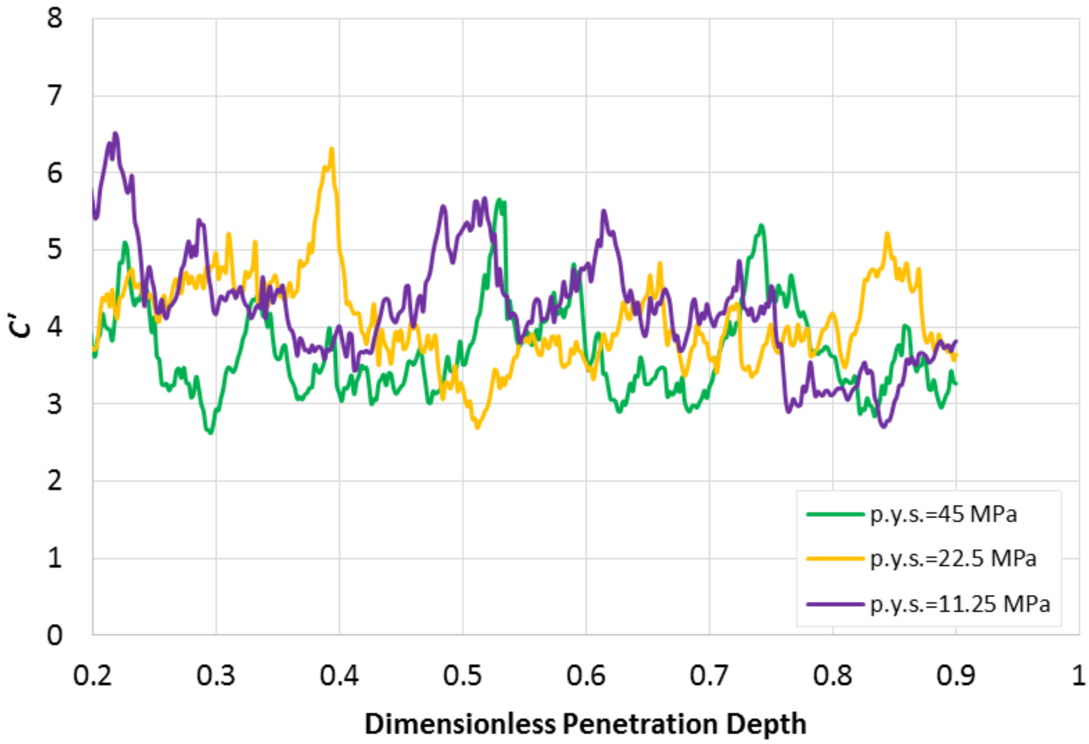

Fig. 24. *C′* against dimensionless penetration depth for three different values of plastic yield stress.

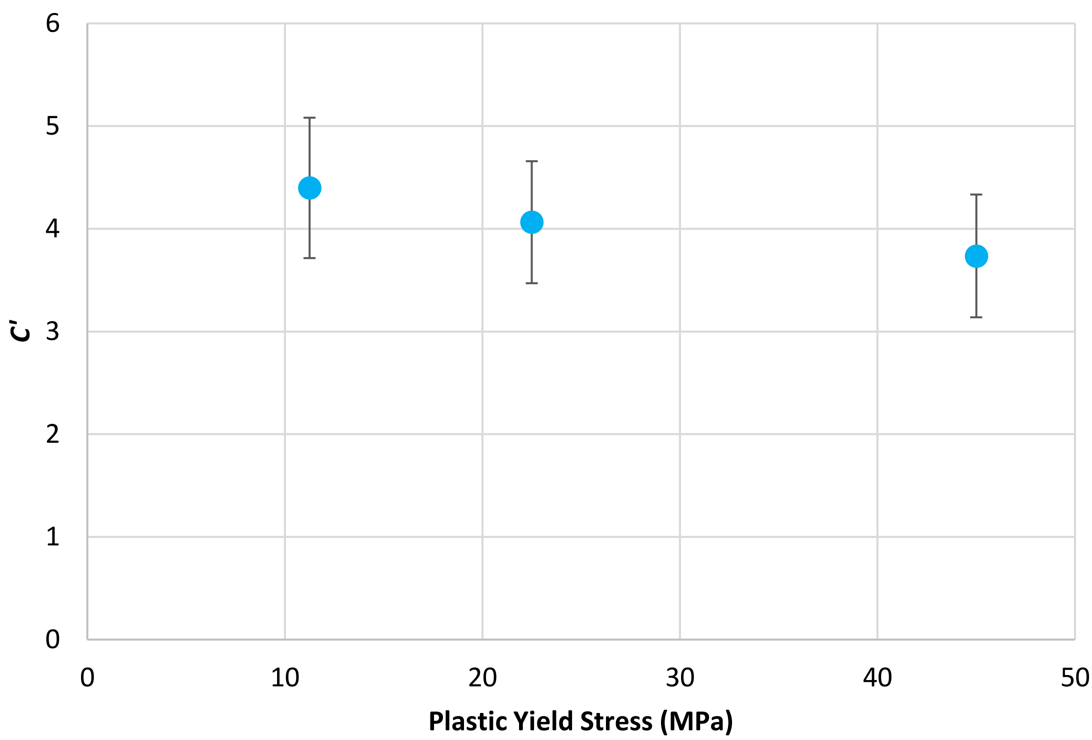

Fig. 25. Average *C′* in the depth range of 0.2 - 0.8 against plastic yield stress.

In both DEM and experiments, fluctuations always arise due to constant rearrangement and deformation of the particle contacts. Throughout all the simulations using the range of properties defined in Table 1, the fluctuations in *C′*, which are predominantly caused by fluctuations in deviatoric stress (e.g. Fig. 23), are of similar magnitude. Comparing to the experimental results of Zafar (2013) it can be seen that the force fluctuations are greater in the DEM simulations. The increased fluctuations in DEM simulations, as compared to experiments, are attributed to the sampling frequency in DEM, 100 Hz in this work, whereas most experimental equipment only provide data at much lower frequencies. Furthermore, real materials usually behave in a more ductile manner than represented in DEM, and hence reduced fluctuations would be expected.

4 Conclusions

The ball indentation method was simulated using DEM. Hardness and localised shear stresses directly beneath the indenter were calculated and the effective constraint factor was determined. Ball indentation simulations at different pre-consolidation stresses in the range of 0.1 - 10 kPa showed that both hardness and the shear stress increased with an increase in pre-consolidation stress, whilst *C′* was found to be independent of the applied pre-consolidation stress. This finding is in agreement with trends previously determined experimentally by Wang *et al.* (2008) and Zafar (2013), however these results demonstrate that this remains the case down to very low stresses, beyond the range that could be determined experimentally.

In addition to this, the influence of a number of particle properties on the exerted stresses and the constraint factor was studied by independently varying each property, in an effort to reach the aim of defining constraint factor as a function of these properties. An increase in interparticle interface energy was shown to lead to an increase in hardness and deviatoric stress, and an increase in the effective constraint factor for relatively cohesionless particles, however the effective constraint factor was found to be independent of interface energy for cohesive particles. An increase of interparticle static friction coefficient resulted in an increase of hardness and shear stress, up to a certain point (μ_s

= 0.3), after which they remained relatively constant, whilst an increased interparticle rolling friction coefficient from 0.01 to 0.05 led to increases in both hardness and deviatoric stress, with a further increase causing them to reduce. The effective constraint factor steadily decreased with increased static friction, although the error bars are noticeable, while it significantly increased when μ_r was increased from 0.05 to 0.1. Lastly, an increase in the plastic yield stress led to a decrease in hardness, though did not influence the deviatoric stress, hence the effective constraint factor was reduced.

Further work is required to fully account for the full range of particle properties which may influence constraint factor. One particular challenge is to determine a suitable shape descriptor to fully account for shape effects.

Acknowledgements

The financial support of the International Fine Particle Research Institute (IFPRI) is gratefully acknowledged. Furthermore, the authors greatly appreciate the MATLAB code provided by Dr. Massih Pasha (The Chemours Company) for the calculation of the input parameters for the DEM contact model used in this work.

References

Alizadeh, M., Asachi, M., Ghadiri, M., Bayly, A. and Hassanpour, A., 2018. A methodology for calibration of DEM input parameters in simulation of segregation of powder mixtures, a special focus on adhesion. *Powder Technology*, *339*, pp.789-800.

Bagi, K., 1996. Stress and strain in granular assemblies. *Mechanics of Materials*, *22*(3), pp.165-177.

Cundall, P.A. and Strack, O.D., 1979. A discrete numerical model for granular assemblies. *Geotechnique*, *29*(1), pp.47-65.

Cundall, P.A., 1971. A computer model for simulating progressive, large-scale movement in blocky rock system. In *Proceedings of the International Symposium on Rock Mechanics, 1971*.

Freeman, R., 2005. Technical Report-Powder Testing-Dealing with the Daily Challenges. *Powder Handling and Processing*, *17*(5), pp.294-296.

Gröger, T. and Katterfeld, A., 2006. On the numerical calibration of discrete element models for the simulation of bulk solids. *Computer Aided Chemical Engineering*, *21*, pp.533-538.

Hare, C. and Ghadiri, M., 2013, June. The influence of aspect ratio and roughness on flowability. In *AIP Conference Proceedings*, *1542*(1), pp. 887-890.

Harnby, N., Hawkins, A.E. and Vandame, D., 1987. The use of bulk density determination as a means of typifying the flow characteristics of loosely compacted powders under conditions of variable relative humidity. *Chemical Engineering Science*, *42*(4), pp.879-888.

Hassanpour, A. and Ghadiri, M., 2007. Characterisation of flowability of loosely compacted cohesive powders by indentation. *Particle & Particle Systems Characterization*, *24*(2), pp.117-123.

Hill, R., 1950. *The mathematical theory of plasticity*. Oxford University Press (Clarendon Press), Oxford, UK.

Höhner, D., Wirtz, S. and Scherer, V., 2014. A study on the influence of particle shape and shape approximation on particle mechanics in a rotating drum using the discrete element method. *Powder Technology*, *253*, pp.256-265.

Jenike, A.W., 1961. Gravity flow of bulk solids. *Bulletin No. 108*, *University of Utah*, *USA*.

Jenike, A.W., 1964. Storage and Flow of Solids. *Bulletin No. 123*, *University of Utah*, *USA*.

Johnson, K.L., 1985. *Contact mechanics*. Cambridge University Press, Cambridge, UK.

Johnson, K.L., Kendall, K. and Roberts, A.D., 1971. Surface energy and the contact of elastic solids. *Proc. R. Soc. Lond. A*, *324*(1558), pp.301-313.

Kozlov, G.V., Serdyuk, V.D. and Beloshenko, V.A., 1995. The plastic constraint factor and mechanical properties of a high-density polyethylene on impact loading. *Mechanics of Composite Materials*, *30*(5), pp.506-509.

Luding, S., 2008. Cohesive, frictional powders: contact models for tension. *Granular Matter*, *10*(4), p.235.

Pasha, M., 2013. *Modelling of flowability measurement of cohesive powders using small quantities*. PhD Thesis, University of Leeds, UK.

Pasha, M., Dogbe, S., Hare, C., Hassanpour, A. and Ghadiri, M., 2014. A linear model of elasto-plastic and adhesive contact deformation. *Granular Matter*, *16*(1), pp.151-162.

Pasha, M., Hare, C., Hassanpour, A. and Ghadiri, M., 2013. Analysis of ball indentation on cohesive powder beds using distinct element modelling. *Powder Technology*, *233*, pp.80-90.

Pasha, M., Hare, C., Hassanpour, A. and Ghadiri, M., 2015. Numerical analysis of strain rate sensitivity in ball indentation on cohesive powder beds. *Chemical Engineering Science*, *123*, pp.92-98.

Rios, M., 2006. Developments in powder flow testing. *Pharmaceutical Technology*, *30*(2).

Schulze, D., 2008. *Powders and bulk solids. Behavior, characterization, storage and flow*. Springer, NY, USA.

Søgaard, S.V., Pedersen, T., Allesø, M., Garnaes, J. and Rantanen, J., 2014. Evaluation of ring shear testing as a characterization method for powder flow in small-scale powder processing equipment. *International Journal of Pharmaceutics*, *475*(1-2), pp.315-323.

Stavrou, A.G., 2019. *Assessing Powder Flowability at Low Consolidation Stresses*. PhD Thesis, University of Surrey, UK.

Tabor, D., 1951. *The hardness of metals*. Oxford University Press (Clarendon Press), Oxford, UK.

Tabor, D., 1996. Indentation hardness: fifty years on a personal view. *Philosophical Magazine A*, *74*(5), pp.1207-1212.

Tardos, G.I., McNamara, S. and Talu, I., 2003. Slow and intermediate flow of a frictional bulk powder in the Couette geometry. *Powder Technology*, *131*(1), pp.23-39.

Thakur, S.C., Ooi, J.Y. and Ahmadian, H., 2016. Scaling of discrete element model parameters for cohesionless and cohesive solid. *Powder Technology*, *293*, pp.130-137.

Thornton, C. and Ning, Z., 1998. A theoretical model for the stick/bounce behaviour of adhesive, elastic-plastic spheres. *Powder Technology*, *99*(2), pp.154-162.

Tomas, J., 2007. Adhesion of ultrafine particles—a micromechanical approach. *Chemical Engineering Science*, *62*(7), pp.1997-2010.

Walton, O.R. and Johnson, S.M., 2009, June. Simulating the Effects of Interparticle Cohesion in Micron-Scale Powders. In *AIP Conference Proceedings*, *1145*(1), pp.897-900.

Wang, C., Hassanpour, A. and Ghadiri, M., 2008. Characterisation of flowability of cohesive powders by testing small quantities of weak compacts. *Particuology*, *6*(4), pp.282-285.

Zafar, U., 2013. *Assessing flowability of cohesive powders by ball indentation*. PhD Thesis, University of Leeds, UK.

Zafar, U., Hare, C., Hassanpour, A. and Ghadiri, M., 2017. Ball indentation on powder beds for assessing powder flowability: Analysis of operation window. *Powder Technology*, *310*, pp.300-306.